Chapter 6

A NDT&E Methodology Based on Magnetic Representation for Surface Topography of Ferromagnetic Materials

Yanhua Sun and Shiwei Liu

Additional information is available at the end of the chapter

http://dx.doi.org/10.5772/62414

Abstract

Accurate evaluation is the final aim of nondestructive testing (NDT). However, the present electromagnetic NDT methods are commonly used to check the existence of defects, and all the tested targets only consist of concave defects (i.e., section-loss defects), such as holes, cracks, or corrosions, failing to evaluate the tested surface topography, which mainly consists of concave-shaped and bump-shaped features. At present, it is accepted that the commonly observed signals of the defects mainly manifest themselves in a single-/double-peak wave and their up/down directions of the peak wave can be easily changed just by changing the directions of either applied magnetization or pick-up units even for one defect. Unlike the present stylus and optical methods for surface topography inspections, a new electromagnetic NDT and evaluation (NDT&E) methodology is provided based on the accurate magnetic representation of surface topography, in which a concave-shaped feature produces "positive" magnetic flux leakages (MFLs) and therefore forms a "raised" signal wave but a bump-shaped feature generates "negative" magnetic fields and therefore leads to a "sunken" signal wave. In this case, the corresponding relationships between wave features and surface topography are presented and the relevant evaluation system for testing surface topography (concave, bumped, and flat features) is built. The provided methodology was analyzed and verified by finite element and experimental methods. Meanwhile, the different dimension parameters of height/depth and width of surface topography are further studied.

Keywords: Nondestructive testing and evaluation (NDT&E), surface topography, non-contact electromagnetic inspection, magnetic representation, dimension parameters, ferromagnetic materials

1. Introduction

Accurate evaluation is the final aim of NDT. However, present electromagnetic NDT methods (i.e., [1]) are commonly used to check the existence of defects, and all the tested targets only consist of concave defects (i.e., section-loss defects), such as holes, slots, break flaws, corrosion pits, notches, and cracks, failing to evaluate the tested surface topography which mainly consists of concave-shaped and bump-shaped features. Particularly, in electromagnetic NDT standards such as the American Society for Testing and Materials (ASTM) E570-09: 2009 (i.e., [2]) and British Standards (BS) EN 10246–4: 2000 (i.e., [3]), and models or specimens in large amounts of research and report. The reference discontinuities only consist of notch, hole, and hole and notch combination types in a standard specimen, as shown in **Figure 1**, as well as the models used in Li Xiao-meng's research on the stress-magnetism effect of ferromagnetic materials based on three-dimensional (3-D) magnetic flux leakage testing [4], Yong Zhang's adaptive method for channel equalization in MFL inspection [5], and Z.D. Wang's review of three magnetic NDT technologies [6], and so on, which are all concave defects. Thus, all the previous work focuses on the inspected objectives of concave defects, and all of the standard specimens for equipment calibration in engineering practice or for experiments or simulations in labs only consist of concave defects. At present, it is accepted that the commonly observed signals of the defects mainly manifest themselves in a single-/double-peak wave, and their up/down directions of the peak wave can be easily changed just by changing the directions of either applied magnetization or pick-up units even for one defect.

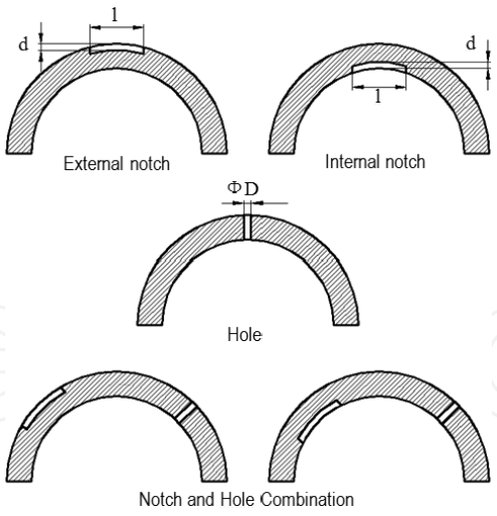

Figure 1. Standard specimens with reference defect consisting of concave-like defects in electromagnetic NDT.

Surface topography usually consists of concave (i.e., section loss), bumped (i.e., section gain), and flat features. At present, there are a number of useful techniques for testing surface topography [7], but three typical methods for detecting surface topography, namely, observation, stylus, and optical methods, are most commonly used in engineering practice [8–19]. The observation method can simply tell which surface is more rough. Although the stylus

http://dx.doi.org/10.5772/62414

method may provide excellent vertical resolution of more than 1 nm, it must contact the test surface. The pressure formed by the contact between the stylus tip and the specimen surface is sufficient to cause permanent damage to a number of common engineering materials especially when used in high-precision roughness measurement, and a limitation for the radius of stylus also exists. The optical approaches would be much better if they are unaffected by some environmental factors such as surface cover or light intensity. In this manuscript, unlike the present stylus or optical methods for surface topography inspections of materials [19–27], a new electromagnetic NDT&E methodology is provided on the basis of the accurate magnetic representation of surface topography. Corresponding relationships between wave features and surface topography are presented and the relevant evaluation system for testing surface topography (concave, bumped, and flat features) is built. The provided methodology is analyzed and verified by finite element and experimental methods. Meanwhile, the different dimension parameters of height/depth and width of surface topography are further studied.

2. NDT&E methodology for surface topography

For a ferromagnetic material, a concave-shaped topography in its surface will produce "positive" magnetic flux leakages due to magnetic refractions, forming a "raised" signal wave. In contrast, a bump-shaped topography will generate "negative" magnetic fields region because of its self-magnetization regulation, leading to a "sunken" signal wave, as illustrated in **Figure 2**.

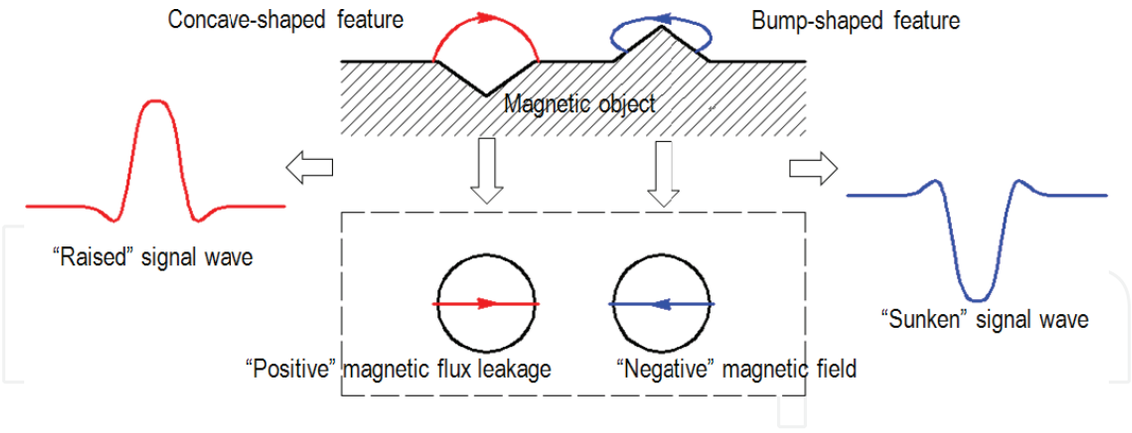

Figure 2. The magnetic representation of surface topography for ferromagnetic materials.

Accordingly, three models, namely triangular concave defects, bump defects, and their multifeature defects (three concave and two bump feature defects), were primarily built for simulations. By using finite element simulations and experimental methods, the magnetic field distribution in the vicinity of both types of defects and their signal waves was obtained, as shown in **Figure 3**, and magnetic scalar potential method was primarily used here. What can be drawn from **Figure 3a** is that the MFL produced by the concave-shaped defects such as cracks and corrosions is an increase, evidently being much stronger than the magnetic field in

the region without any defects. In contrast, from **Figure 3c**, it can be seen that bump-shaped defects like protrusions produce an opposite/converse/negative magnetic field and thereafter forms a decrease vicinity of it as excepted. As a result, all picking-up (or measuring) points for magnetic field density near the concave defect are much stronger and finally a raised signal wave is formed. Conversely, those near the bump defect are much weaker and finally a sunken signal wave is formed, as shown in **Figure 3b** and **3d**, respectively. Finally, a continuous set of multifeature defects including concave and bump are modeled and simulated as shown in **Figure 3e**, and the signal of magnetic flux density above the surface of ferromagnetic material object is shown in **Figure 3f**, which constitutes a succession of raised and sunken features and directly reflects the defects.

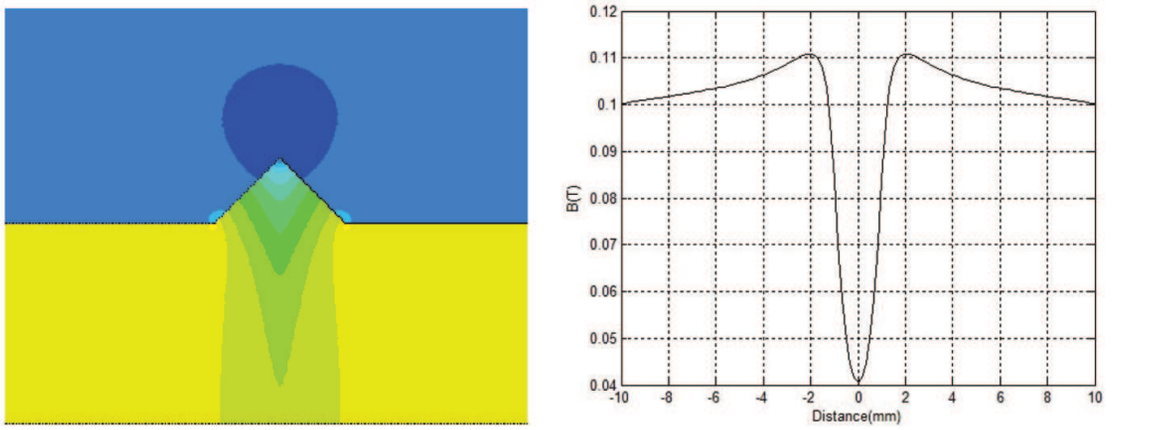

(c) MFL produced by bump-shaped defects (d) Sunk signal wave formed by bump-shaped defects

(e)MFL produced by multi-feature defects (f) continuous raised and sunk signals by multi-feature defects

Figure 3. Magnetic representation of concave-shaped and bump-shaped topography. (a) MFL produced by concave-shaped defects (b) Raised signal wave formed by concave-shaped defects (c) MFL produced by bump-shaped defects (d) Sunk signal wave formed by bump-shaped defects (e)MFL produced by multi-feature defects (f) continuous raised and sunk signals by multi-feature defects.

From the perspective of geometry, surface topography is composed by a series of micro concave-shaped defects/features and bump-shaped defects/features. Therefore, if these two

http://dx.doi.org/10.5772/62414

types of features are inspected, surface topography can also be easily measured accordingly. In this case, by using magnetic sensors to directly induce the magnetic features with a certain liftoff distance above the measured surface, the corresponding surface topography can be inspected and therefore be evaluated [28–45]. Naturally, a non-contact magnetic inspection and evaluation methodology is provided here by using magnetic sensors such as Halls or magneto-resistive units with a certain liftoff distance to directly scan the corresponding magnetic characters caused by different surface topography, concave or bump, for instance, and then, the picking-up signals are processed through a data processing system where the surface topography is reflected ultimately, as shown in **Figure 4**.

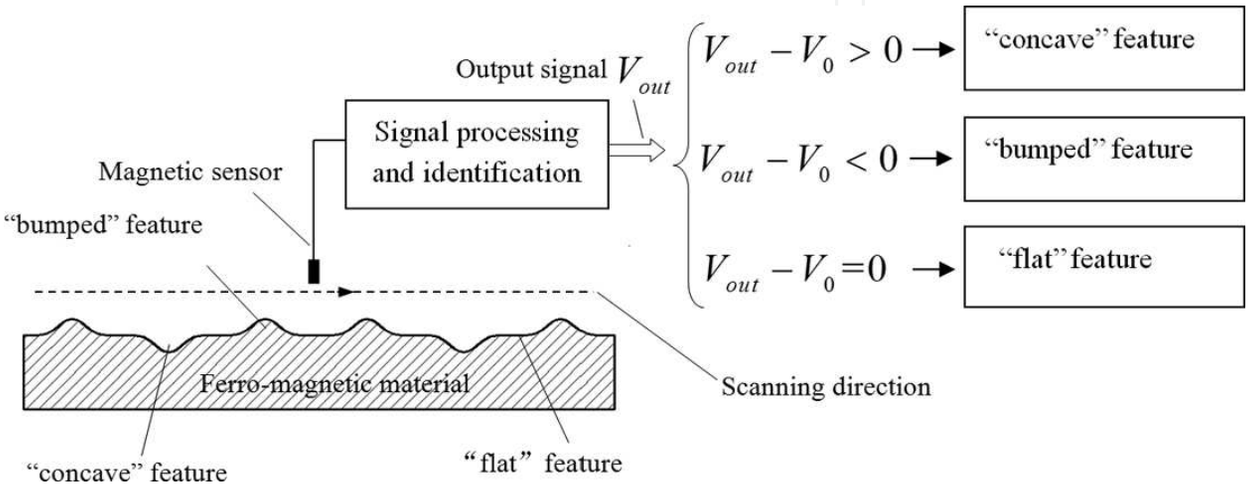

Figure 4. Non-contact magnetic inspection and evaluation methodology for surface topography.

The judgment of the output signals is completed by formulas (1)–(3), where V_{out} is the output voltage signal of magnetic sensor and V_0 represents the baseline voltage. When formula (1) is satisfied, we can definitely consider appearance of a concave feature. Similarly, bumped features and flat features can be indentified or inspected as formulas (2) and (3) are met, respectively. As usual, the residual magnetism in the inspected object is introduced by some manufacturing processes. Even if there is no residual magnetism, applying magnetization also can be easily done.

$$V_{out} - V_0 > 0 \tag{1}$$

$$V_{out} - V_0 < 0 \tag{2}$$

$$V_{out} - V_0 = 0 \tag{3}$$

Using the given inspection method, ferromagnetic material surface topography can be scanned and reflected by output signals; most importantly, the proposed inspection method is unaf-

fected by other external elements such as surface perfection and light intensity. Here, the key issue is to confirm the different generating mechanisms of the two classified defects through their apparently different signal features.

3. Simulations

To implement the finite element simulation, a 2-D axisymmetric model is built in ANSYS. The simulation model consists of a pipe to show the signal characteristics of concave and convex, a coil used to magnetize the pipe, and a surrounding air region to conduct the magnetic field. All the models are meshed with PLANE 53 elements, which are commonly used in electromagnetic analyses. To precisely and quantitatively test the surface topography, the studies for the parameters of height/depth and width were also simultaneously and systematically included. Concaves and convex are meshed with elements of size 0.04 mm and other regions are meshed with elements of size 0.2 mm. Flux-parallel boundary condition is applied to the exterior nodes to confine the magnetic field inside the air region. Magnetizing current density of the coil is set to 1×10^7 A/m^2. After solving, a path is drawn above the pipe surface to extract the magnetic field distribution and show the MFL signal. To be specific, the dimension parameters of height/depth and width of surface topography were further studied, where the scalar magnetic potential method was primarily applied. According to the non-contact magnetic inspection method proposed here, three basic models were built, namely, triangular

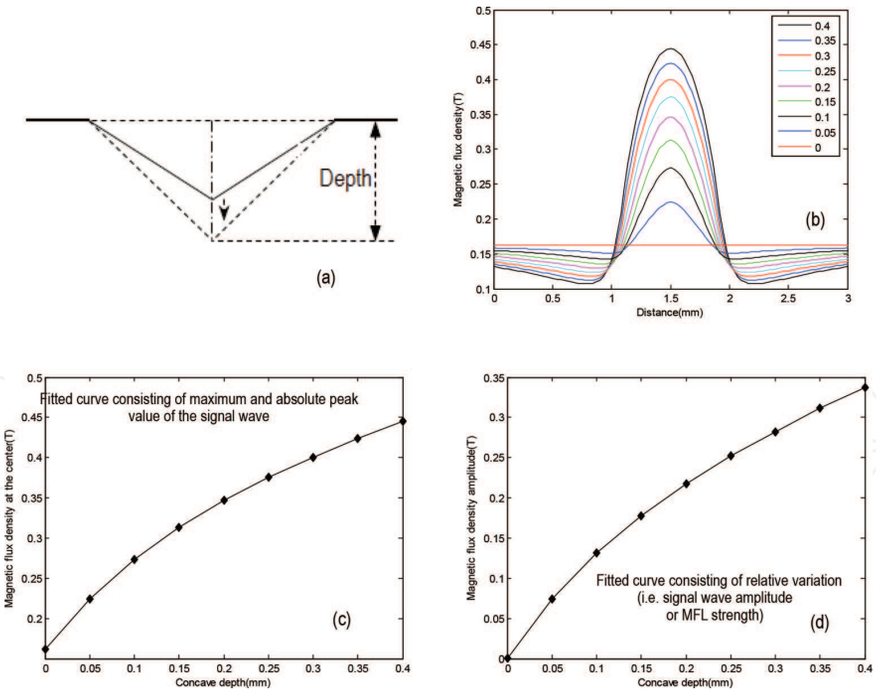

Figure 5. Detailed FEM results by separately varying the depth of the triangular "concave" defect. (a) schematic model of concave depth in simulation; (b) MFL signals in different "concave" depth; (c) Fitted curve consisting of maximum and absolute peak value of the signal wave(d) Fitted curve consisting of relative variation (i.e. signal wave amplitude or MFL strength).

http://dx.doi.org/10.5772/62414

"concave" defects (maximum width: 0.8 mm and maximum depth: 0.4 mm), triangular "bump" defects (maximum width: 0.8 mm and maximum height: 0.4 mm), and their multi-feature defects (three "concave" and two "bump" feature defects with the same maximum sizes), with the variable depth/height or width, as schematically illustrated in **Figures 5a–9a**, respectively. To summarise, the key characters of both the triangular "concave" defect and the "bump" defect are in accordance with the analyses mentioned previously. That is, the former generates "positive" MFL (i.e., an increase) but the latter forms "negative" magnetic field (i.e., a decrease), resulting in a raised test signal wave and a sunken wave, respectively.

Concretely, in **Figure 5a**, by separately varying the depth of the triangular "concave" defect with the decreasing unit of 0.05 mm per step (from 0 to 0.4 mm), a series of raised signal waves were generated as indicated in **Figure 5b**. The resulting fitted curve consisting of maximum and absolute magnetic flux density in the vicinity of the center of the defect (i.e., the maximum and absolute peak value of the signal wave) and the fitted curve consisting of relative variation (i.e., signal wave amplitude representing MFL strength) are displayed in **Figure 5c** and **5d**, respectively.

From **Figure 5**, it can be observed that the "positive" magnetic flux density in the vicinity of the "concave" defect is larger than that far away from the defect and increases with the increasing depth of the defect in approximately linear form. Briefly speaking, we can conclude that the signal wave amplitude (or the MFL strength) is approximately proportional to the depth linearly.

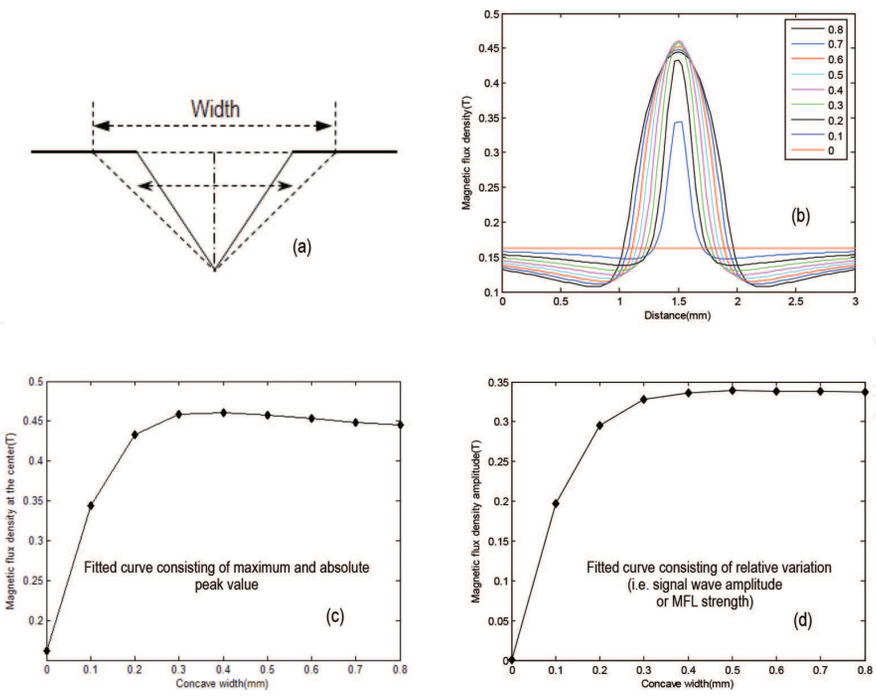

Figure 6. Detailed FEM results by separately varying the width of the triangular "concave" defect. (a) schematic model of concave width in simulation; (b) MFL signals in different "concave" width; (c) Fitted curve consisting of maximum and absolute peak value; (d) Fitted curve consisting of relative variation (i.e. signal wave amplitude or MFL strength).

On the other hand, in **Figure 6a**, by separately changing the width of the triangular "concave" defect with the decreasing unit of 0.1 mm per step (from 0 to 0.8 mm), the series of raised signal waves were also obtained as shown in **Figure 6b**. Likewise, the fitted curve consisting of maximum and absolute magnetic flux density in the vicinity of the center of the defects (i.e., the maximum and absolute peak value of the signal wave) and the fitted curve consisting of relative variation (i.e., the signal wave amplitude displaying the MFL strength) are given in **Figure 6c** and **6d**, respectively.

Which can be shown from **Figure 6** is that the amplitude of the "positive" magnetic flux density produced by the "concave" defect increases with the increasing depth in a nonlinear form, growing more rapidly at smaller value of width but decreasing gradually at higher value. That is, the signal wave amplitude (or the MFL strength) increases rapidly at first but then gradually decreases as the width grows. Most notably, the decrease of amplitude is limited and remains at a high level approaching the maximum value (i.e., peak value) during the whole change process.

Similarly, as demonstrated in **Figure 7a**, by separately varying the height of the triangular "bump" defect with the decreasing unit of 0.05 mm per step (from 0 to 0.4 mm), a series of sunken signal waves were obtained, as displayed in **Figure 7b**, and so did the fitted curve consisting of minimum and absolute magnetic flux density in the vicinity of the center of the defect (i.e., the minimum and absolute peak value of the signal wave) and the fitted curve consisting of relative variation (i.e., signal wave amplitude demonstrating the "negative" magnetic strength), as shown in **Figure 7c** and **7d**, respectively.

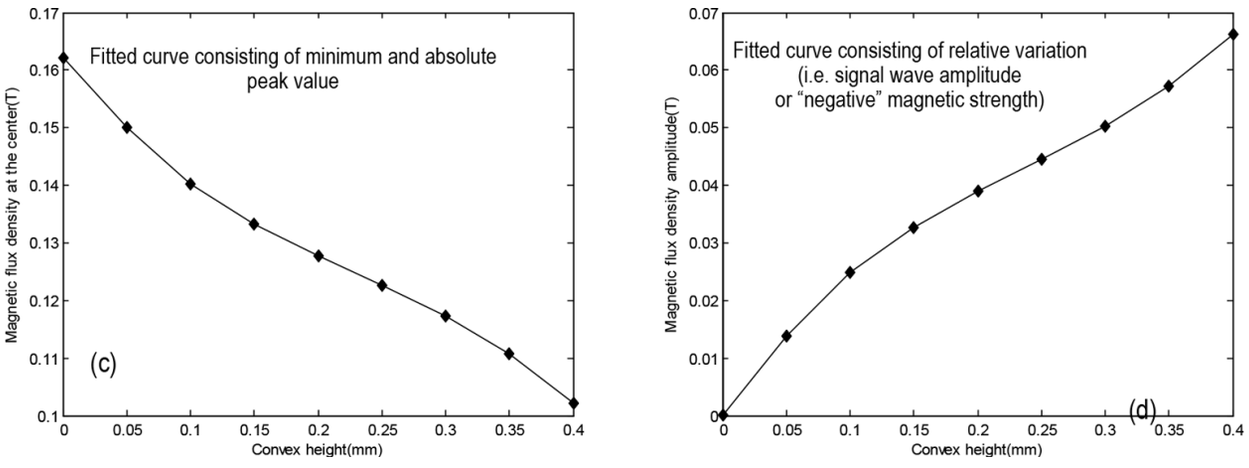

Figure 7. Detailed FEM results by separately varying the height of the triangular "bump" defect. (a) schematic model of bump height in simulation; (b) MFL signals in different "bump" height; (c) Fitted curve consisting of minimum and absolute peak value (d) Fitted curve consisting of relative variation (i.e. signal wave amplitude or "negative" magnetic strength).

Conversely, from **Figure 7**, it can be concluded that the sunken signal wave amplitude (i.e., peak-to-peak value indicating the "negative" magnetic strength) grows as the height of the triangular defect increases. In particular, **Figure 7c** intuitively demonstrates that the higher the

http://dx.doi.org/10.5772/62414

"bump" defect is, the weaker the absolute magnetic field strength in the vicinity of the defect is, which also displays the existence of the "negative" magnetic fields.

Similarly to **Figure 6**, in **Figure 8a**, by separately varying the width of the triangular "bump" defect with the decreasing unit of 0.1 mm per step (from 0 to 0.8 mm), a series of concave-like signal waves were also obtained as presented in **Figure 8b**, and the fitted curve consisting of maximum and absolute magnetic flux density in the vicinity of the center of the defect (i.e., the minimum and absolute peak value of the signal wave) and the fitted curve consisting of relative variation (i.e., signal wave amplitude demonstrating the "negative" magnetic strength) are also obtained, intuitively displayed in **Figure 8c** and **8d**, respectively.

The results from **Figure 8** reveal the similar change trend from **Figure 7**, concerning the relationship between the amplitude of signal waves (indicating the "negative" magnetic strength) and the variable width of the defect. That is, the sunken signal wave amplitude (i.e., peak-to-peak value indicating the "negative" magnetic strength) increases with the increasing height of the triangular defect. However, compared with the results obtained from **Figure 6**

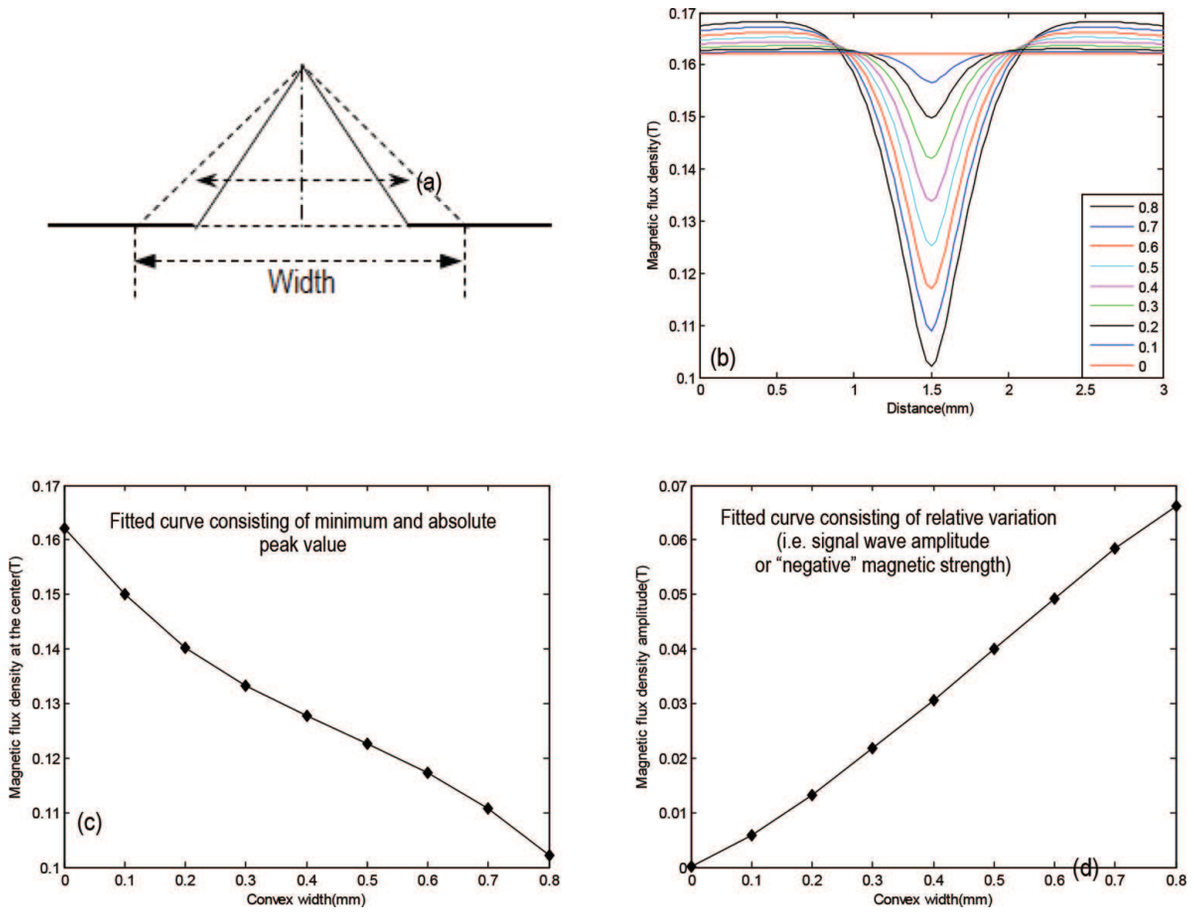

Figure 8. Detailed FEM results by separately varying the width of the triangular "bump" defect. (a) schematic model of bump width in simulation; (b) MFL signals in different "bump" width; (c) Fitted curve consisting of minimum and absolute peak value (d) Fitted curve consisting of relative variation (i.e. signal wave amplitude or "negative" magnetic strength).

illustrating the effect caused by the variable width, the linear relationship between the signal amplitude and the defect width is better in **Figure 8**.

Finally, in a like manner, the finite element modeling (FEM) results for the multifeature defects (three "concave" and two "bump" feature defects with the same maximum sizes) were obtained, as shown in **Figure 9**, from which the similar relationships between the signal amplitudes and the depth/height and width can be observed, and it can be concluded that the sensitivity of the identification can at least reach 0.02 mm in height and 0.02 mm in width of the defect. Actually and theoretically, the smaller features ("concave" or "bump") can be observed through the mechanisms. To be more concrete, **Figure 9a** and **9c** presents the variable height/depth and width in multifeature defects model, respectively, while **Figure 9b** and **Figure 9d** displays the MFL signals correspondingly.

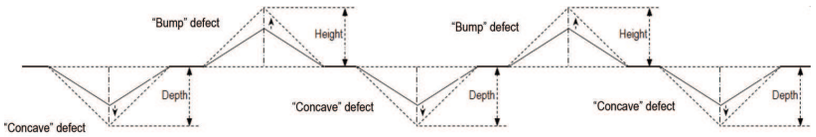

(a) Multi-feature defects of height/depth

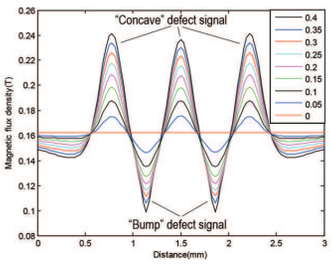

(b) Testing signals of multi-feature defects for height/depth

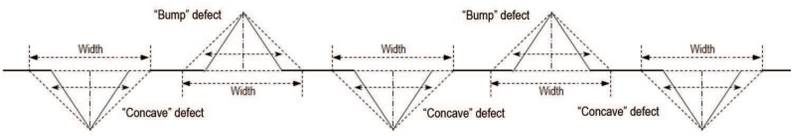

(c) Multi-feature defects of width

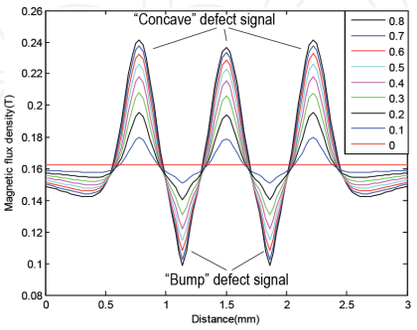

(d) Testing signals of multi-feature defects for width

Figure 9. Detailed FEM results for the multifeature defects (three "concave" and two "bump" feature defects with the same maximum sizes). (a) Multi-feature defects of height/depth (b) Testing signals of multi-feature defects for height/depth (c) Multi-feature defects of width (d) Testing signals of multi-feature defects for width.

http://dx.doi.org/10.5772/62414

In addition, finite element modeling (FEM) simulations for multifeature defect (four "concave" and three "bump" features with the same sizes) distance or spacing are also applied, as illustrated in **Figure 10**. Eight kinds of models were simulated with different defect distances or spacing in the process of FEM, as shown in **Figure 10a**. Three "bump" defects and four "concave" defects are evenly spaced with the same distance value of D in every defect simulation model, and the defect distance is, respectively, 0.01, 0.02, 0.04,0.05, 0.065, 0.08, 0.10, and 0 mm, which refers to a smooth surface without any defects in different simulation models. The FEM results are distinctly shown in **Figure 10b**, where each line represents the corresponding MFL signals in the defect distance or spacing simulation.

From the MFL signals observed in **Figure 10b**, an interesting phenomenon can be seen in that magnetic flux density of multifeature defects with different distances are still able to be distinguished from each other, and based on which a conclusion can also be drawn that a defect distance or spacing resolution of 0.01 mm or higher can be reached using this proposed method of surface topography evaluation by electromagnetic methodology.

Equations (1–3) are the basic principal models for the judgment method of "concave," "bumped," and "flat" features in the proposed electromagnetic non-contact method. Certainly, the surface of the object to be tested is scraggly and has the features with different sizes and shapes. Based on the analyses of test signal amplitude displaying the features with different sizes in the manuscript and also as shown above, the different sizes or shapes affect the signal amplitude and thereafter represent surface roughness. Given a constant liftoff distance, the "bump," "concave," and "flat" test signals to be observed for presenting the surface status are

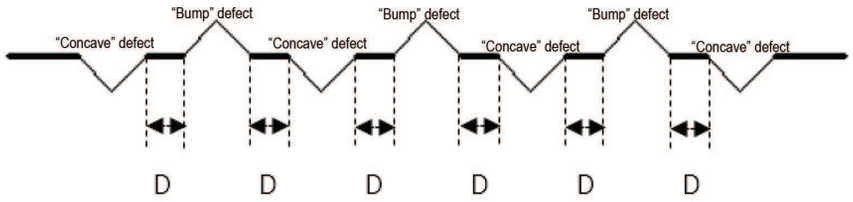

(a) Multi-feature defects of distance

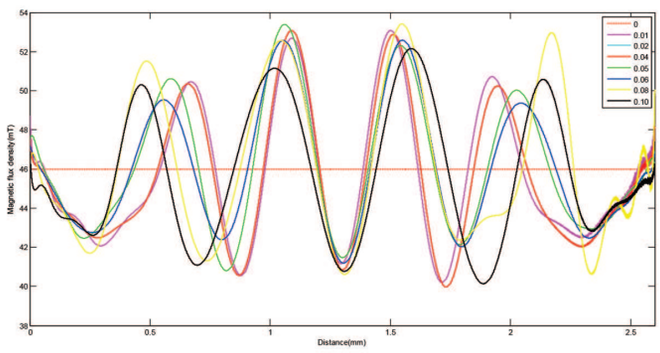

(b) Testing signals of multi-feature defects for distance

Figure 10. Detailed FEM results for the multifeature defect distance (four "concave" and three "bump" features with same sizes). (a) Multi-feature defects of distance (b) Testing signals of multi-feature defects for distance.

exactly due to the various features such as different sizes and shapes. The proposed non-contact test principle is illustrated in **Figure 11**.

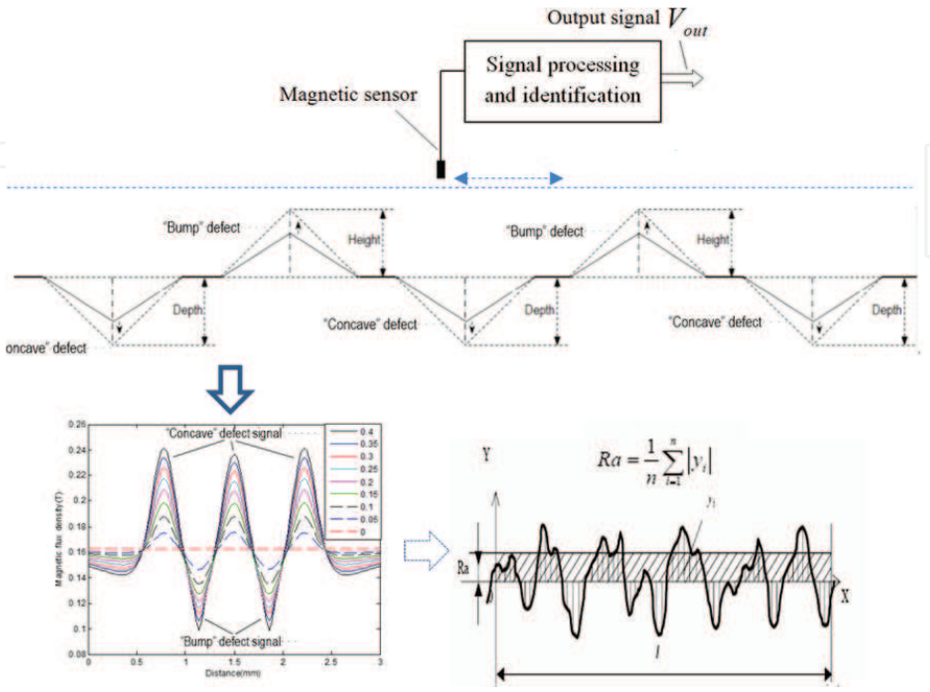

Figure 11. The explanation for non-contact test method at a given liftoff distance of magnetic sensor.

To further and better understand the principles of MFL generating mechanism for surface topography of ferromagnetic materials, three-dimensional FEM simulation was completed. The simulation model containing both "concave" and "bump" defects with magnetic field distribution in 3-D is shown in **Figure 12**. **Figure 12a** expressed simulation model of two typical kinds of defects with certain distances from each other, while **Figure 12b** represents local MFL signals of simulation model in **Figure 12a** and provides basic reference data for surface roughness evaluation, from which we can clearly see that the "concave" and "bump" feature inversely.

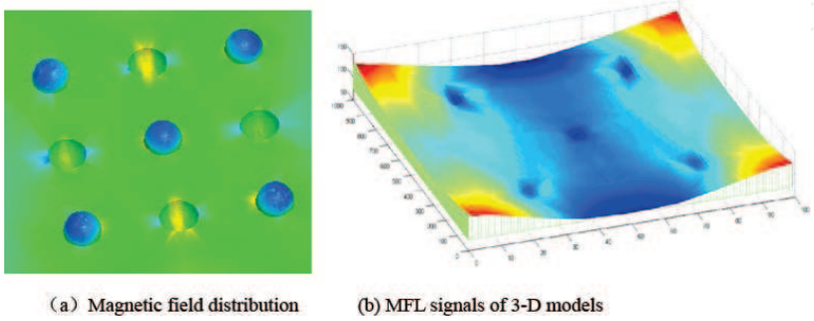

Figure 12. Surface roughness inspection and its signals (3D).(a) Magnetic field distribution (b) MFL signals of 3-D models.

http://dx.doi.org/10.5772/62414

4. Experiments

To further confirm the validity of the non-contact magnetic inspection method,large amount of experiments were performed. According to the simulation models, four kinds of samples were applied in these experiments including triangular concave depth/width and triangular bump height/width. The experimental apparatus and process are briefly shown in **Figure 13** and its procedure and details will be described as follows. First, two groups of magnetizing coils connected by a Hall sensor are driven by electro magnetization and scanning drive modules, which provide magnetizing current and motor power and thus artificial defects on samples made of steel plate can be scanned. Then, defects signals sampled by acquisition card are sent to PC and finally processed and calculated where filtering and amplification are included.

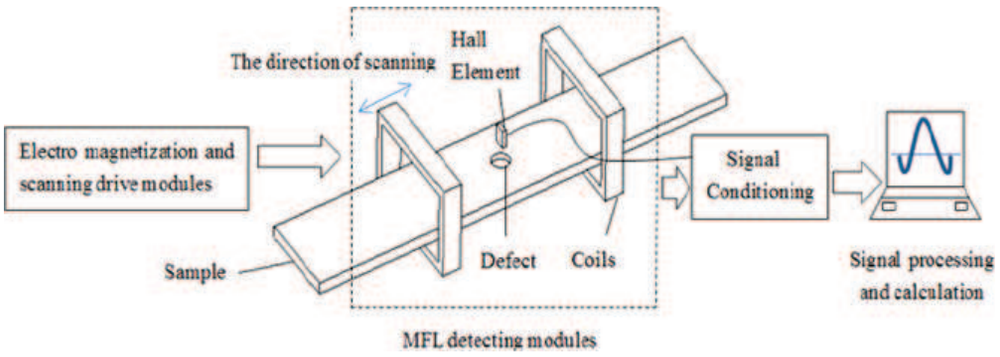

Figure 13. Experimental apparatus and process.

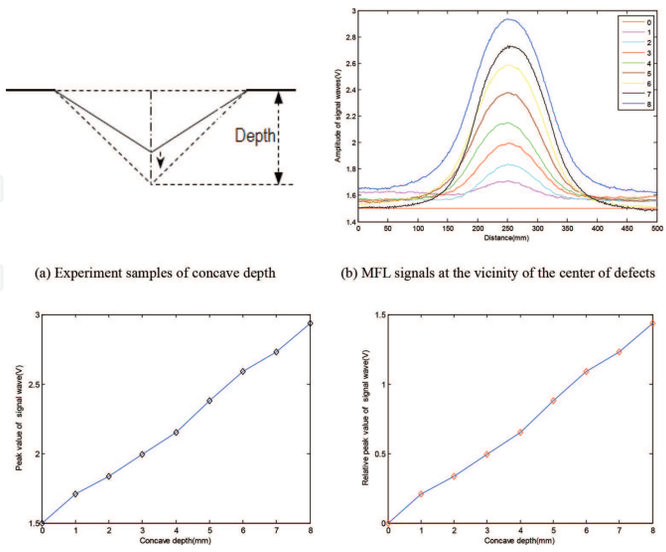

Figure 14. Experimental results for depth variation of triangular concave defects. (a) Experimental samples of concave depth (b) MFL signals in the vicinity of the center of defects. (c) Maximum or absolute peak value of MFL signal wave in (b). (d) Relative peak value of the signal wave in (b).

By scanning at the center in the vicinity of different depth of triangular defects as shown in **Figure 14a**, a series of raised MFL signals were generated as displayed in **Figure 14b** where the legend of 0–8 represents the defect depth of 0–0.4 mm with the increasing unit of 0.05 mm per step. Through calculating the maximum or absolute peak value and the relative peak value of the signal wave in **Figure 14b**, a battery of eigenvalues was acquired as displayed in **Figure 14c** and **14d**, respectively.

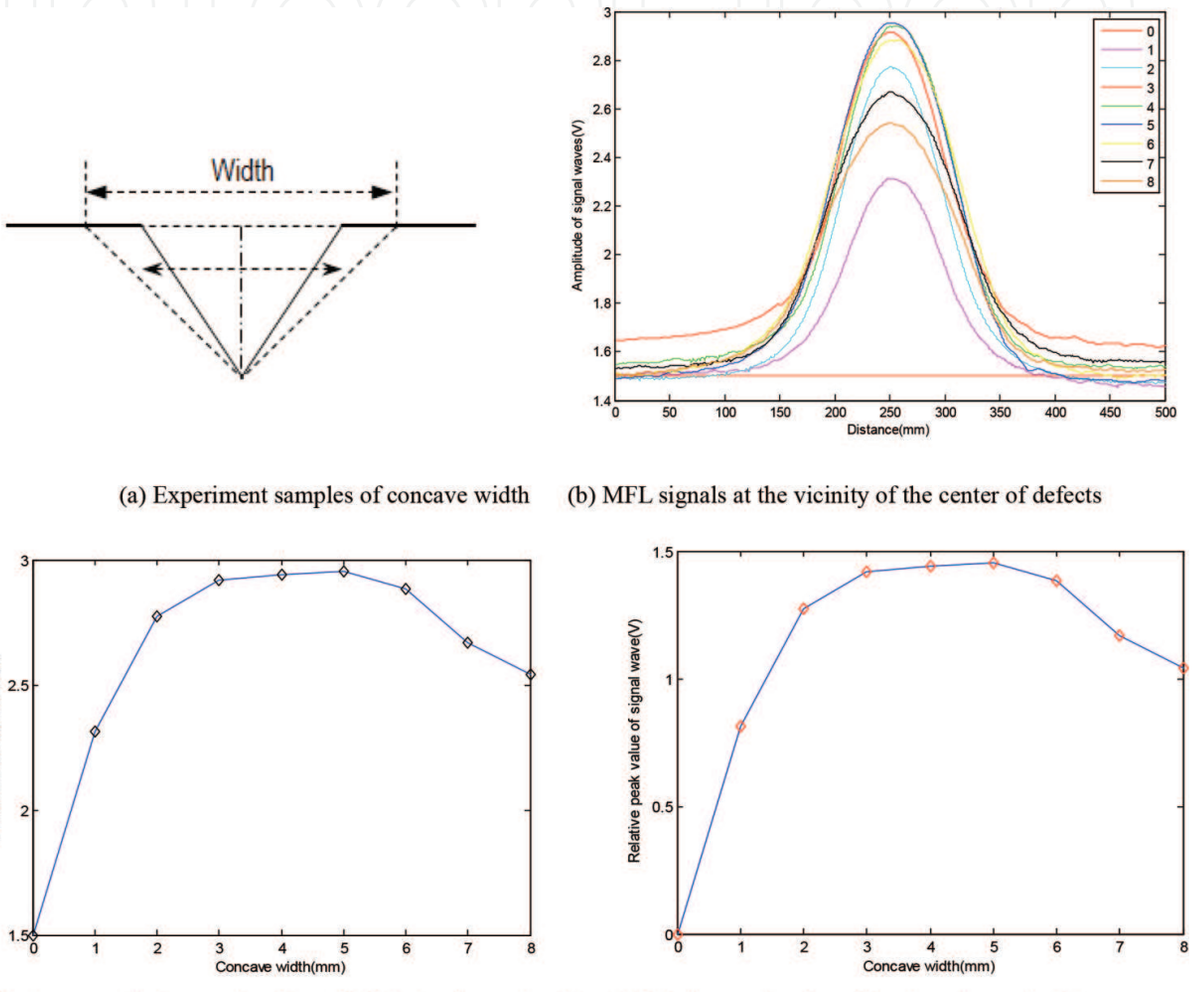

(a) Experiment samples of concave width (b) MFL signals at the vicinity of the center of defects

(c) Maximum or absolute peak value of MFL signal wave in (b) (d) Relative peak value of the signal wave in (b)

Figure 15. Experimental results for width variation of triangular concave defects. (a) Experimental samples of concave width. (b) MFL signals in the vicinity of the center of defects. (c) Maximum or absolute peak value of MFL signal wave in (b). (d) Relative peak value of the signal wave in (b).

Comparing the above experimental results with what has been done in the simulations part, it is not hard to find that the "positive" magnetic flux density in the vicinity of the center of concave defect is larger than that far away from the defect and manifests a similar change trend regarding relevant eigenvalues of maximum and relative peak values. By the consistency of simulations and experimental results, we can definitely conclude that the maximum or the relative peak value is approximately proportional to the concave depth linearly.

http://dx.doi.org/10.5772/62414

By the same token, another experiment was conducted on the samples of width of concave defects. After scanning above the surface of defects as shown in **Figure 15a**, a series of MFL signal waves were presented in **Figure 15b**, in which the legend of 0–8 presents the changing width of triangular concave defect from 0 to 0.8 mm with the increasing unit of 0.1 mm per step. After data processing, the maximum or absoLute Peak Value And The Relative Peak value of the signal wave in **Figure 15b** were acquired and displayed in **Figure 15c** and **15d**, respectively.

Observing from the changing trend of MFL signals of concave width defects and comparing them with the simulation results obtained previously, we can notice that the peak value of MFL signal waves increases rapidly with concave width at the beginning within a small range and remains at a high level as the width increases further. These changing rules are in well accordance with that of the simulations, which further demonstrates the correctness of the relationship between concave width and the peak value of signal waves and provides us the necessary information to predict the defect widths in turn.

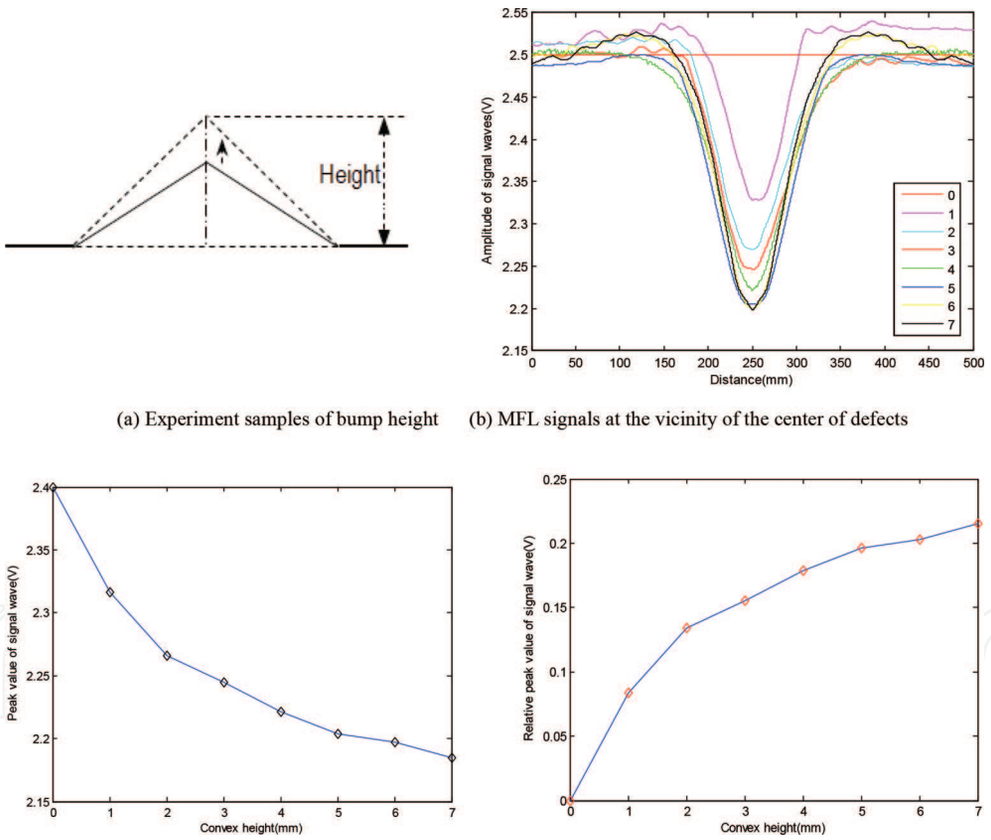

Figure 16. Experimental results for height variation of triangular bump defects. (a) Experimental samples of bump height (b) MFL signals in the vicinity of the center of defects (c) Maximum or absolute peak value of MFL signal wave in (b) (d) Relative peak value of the signal wave in (b).

Likewise, after scanning on the surface of the bump height samples shown in **Figure 16a** with a certain liftoff for the Hall sensor, MFL signal waves representing different values of bump height are expressed in **Figure 16b** where the legend of 0–7 reflects the bump heights of 0–0.35

mm with the increasing unit of 0.05 mm per step. After extracting eigenvalues for the signal waves in **Figure 16b**, the maximum or absolute peak value and the relative peak value of the signal wave in **Figure 16b** were acquired and displayed in **Figure 16c** and **16d**, respectively.

Reading from **Figure 16** and comparing it with simulations of **Figure 7** described earlier, it is obvious that the experimental results about the bump height are in good agreement with the simulations, all of which indicated the existence of the "negative" magnetic fields. Moreover, the parallel change trend also means the presence of a negative correlation between bump height and the peak value of MFL signal wave.

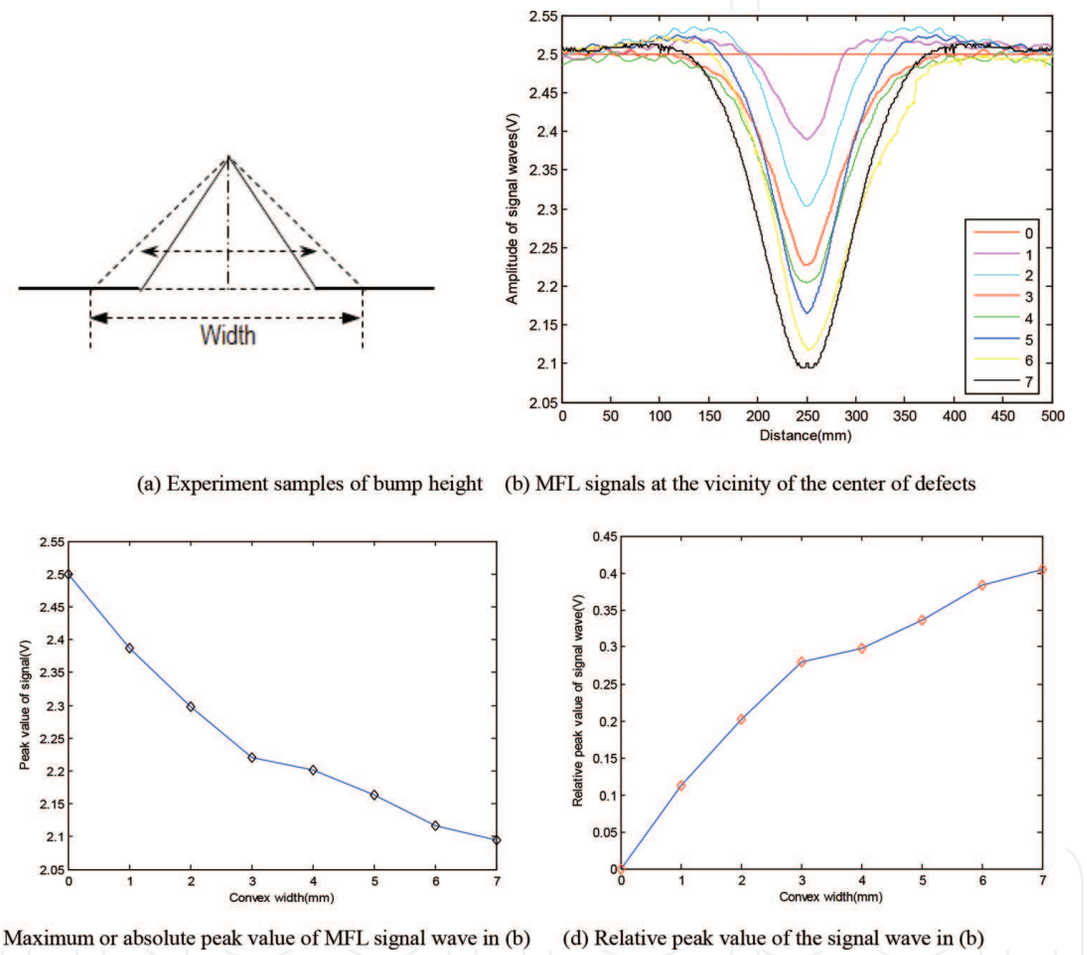

Figure 17. Experimental results for width variation of triangular bump defects. (a) Experimental samples of bump height (b) MFL signals in the vicinity of the center of defects (c) Maximum or absolute peak value of MFL signal wave in (b) (d) Relative peak value of the signal wave in (b).

Similarly, after scanning on the surface of the bump/convex width samples shown in **Figure 16a** with a certain liftoff by the Hall sensor, MFL signal waves representing different values of bump width are expressed in **Figure 16b** where the legend of 0–7 reflects the bump width of 0–0.7 mm with the increasing unit of 0.1 mm per step. After extracting eigenvalues for the signal waves in **Figure 16b**, the maximum or absolute peak value and the relative peak value of the signal wave in **Figure 16b** are acquired and displayed in **Figure 16c** and **16d**, respectively.

http://dx.doi.org/10.5772/62414

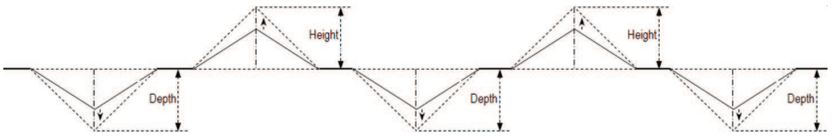

(a) Multi-feature defects of height/depth

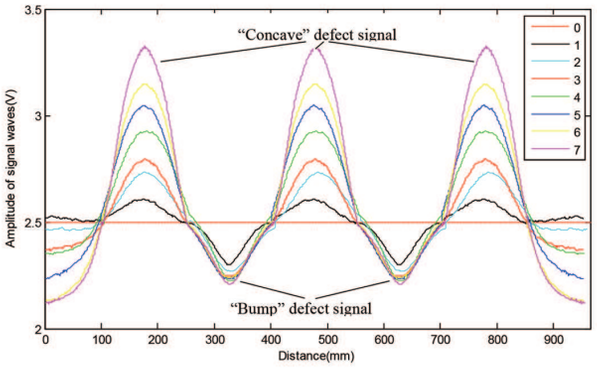

(b) Experiment results of multi-feature defects for height/depth

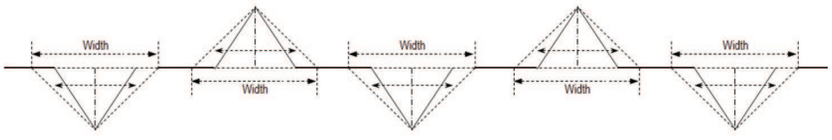

(c) Multi-feature defects of width

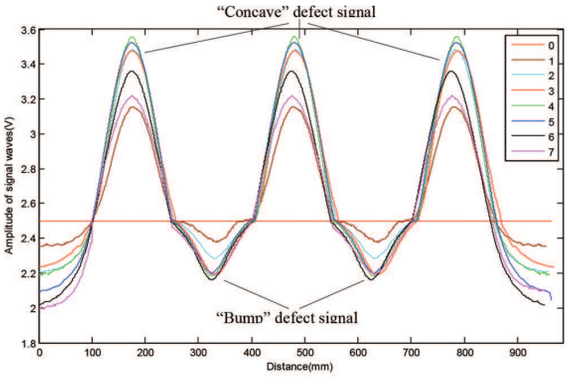

(d)Experiment results of multi-feature defects for width

Figure 18. Experiment results for the multi-feature defects (three "concave" and two "bump" feature defects with the same maximum sizes) (a) Multi-feature defects of height/depth (b) Experiment results of multi-feature defects for height/depth (c) Multi-feature defects of width (d)Experiment results of multi-feature defects for width.

Similarly to explanations for **Figure 16**, observing from **Figure 17(a)–(d)** and comparing it with simulation results of **Figure 8** described earlier, it is obvious that the experimental results about the bump width are in good agreement with the simulations; they indicate not only the existence of the "negative" magnetic fields but also the presence of a negative correctness relation between bump width and peak values of the MFL signal or relative peak values. To be specific, there exists a negative correlation between convex-shaped defect width and peak value of MFL signals, and vice versa for relative peak value of MFL signals. By the measured linear relationship between convex height and signal peak value or relative signal peak value,

convex-shaped defect height can be attained if another variable of MFL signal is obtained in advance.

To verify the validity of the theory proposed in this paper and the reliability of the simulations done previously, experiments for multifeature defects, which include concave and bump defects simultaneously, were also conducted. One group of experimental samples are roughly drawn as shown in **Figure 18a**, where two same concave defect depth and three same bump defect heights vary from 0 to 0.7 mm with an increasing unit of 0.1 mm per step while other dimensions of these defects remain unchanged. Similarly, **Figure 18c** expresses another group of samples that double same concave-shaped defect widths vary with another three same bump defects from 0 to 0.7 mm while other size of these defects remain unchanged. The experimental results are separately shown in **Figure 18b** and **18d**, where the legend of 0–7 represents the variable value of 0–0.7 mm, which coincides well with simulation results in **Figure 9**, as well as further confirming the conclusion of the theory proposed here that a concave-shaped feature will produce "positive" magnetic flux leakages and form a "raised" signal wave while a bump-shaped feature will generate "negative" magnetic fields and lead to a "sunken" signal wave.

To summarise, surface topography or topography measurement can be divided into the measurement of concave and bump features. The combination of simulations and experiments simultaneously demonstrate the correctness and feasibility of the proposed method and the validity of the law that concave-shaped and bump-shaped features possess opposite magnetic field or magnetic flux leakage, and form raised and sunken signal waves, respectively. The change rules of depth/height and width further provided us detailed information about the relationship between surface topography and MFL signal eigenvalues.

5. Conclusions

The up/down directions of the peak wave of the commonly observed signals relate to not only the directions of either applied magnetization or pick-up units but also actually bear on the accurate magnetic representation of surface topography. The corresponding relationships between wave features of observed signals and surface topography features exist. That is, a concave-shaped feature produces "positive" magnetic flux leakages and therefore forms a "raised" signal wave but a bump-shaped feature generates "negative" magnetic fields and therefore leads to a "sunken" signal wave. The provided NDT&E methodology based on magnetic representation for surface topography of ferromagnetic materials is feasible (a raised signal wave representing a concave feature, a sunken signal wave representing a bumped feature, and a baseline wave representing a flat feature), and hopefully the further exploration of its applications can be further done. Surface topography can be accurately tested and evaluated by the provided methodology and the further relationship between signal wave amplitudes and surface parameters such as depth and width.

This study was funded by the National Natural Science Foundation of China (NNSFC) [Project No. 51475194] , the National Key Basic Research Program of China [Project No. 2014CB046706] and National Natural Science Foundation of China(NNSFC) [Project No. 51275193].

http://dx.doi.org/10.5772/62414

Author details

Yanhua Sun* and Shiwei Liu

*Address all correspondence to: yhsun@hust.edu.cn

Huazhong University of Science and Technology, Wuhan, China

References

[1] De Levie, R.: The influence of surface topography of solid electrodes on electrochemical measurements. Electrochimica Acta, 10(2): 113–130 (February 1965).

[2] ASTM E570-09, Standard Practice for Flux Leakage Examination of Ferromagnetic Steel Tubular Products, ASTM International, West Conshohocken, PA, 2009, DOI: 10.1520/E0570-09.www.astm.org.

[3] BS EN 10246–4.: Non-destructive testing of steel tubes – Part 4: Automatic full peripheral magnetic transducer/flux leakage testing of seamless ferromagnetic steel tubes for the detection of transverse imperfections. May (2007). http://www.freestd.us/soft/145444.htm.

[4] L. Xiao-meng, D. Hong-sheng, and B. Shi-wu, "Research on the stress-magnetism effect of ferromagnetic materials based on three-dimensional magnetic flux leakage testing," NDT & E International, vol. 62, pp. 50-54, 2014.

[5] Y. Zhang, Z. Ye, and X. Xu, "An adaptive method for channel equalization in MFL inspection," NDT & E International, vol. 40, pp. 127-139, 2007.

[6] Z. Wang, Y. Gu, and Y. Wang, "A review of three magnetic NDT technologies," Journal of Magnetism and Magnetic Materials, vol. 324, pp. 382-388, 2012.

[7] P. Benardos and G.-C. Vosniakos, "Predicting surface roughness in machining: a review," International journal of machine tools and manufacture, vol. 43, pp. 833-844, 2003.

[8] Poon, C.Y., Bhushan, B.: Comparison of surface topography measurements by stylus profiler, AFM and non-contact optical profiler. Wear, 190(1): 76–88 (November 1995).

[9] Vorburger, T.V., Teague, E.C.: Optical techniques for on-line measurement of surface topography. Precis Eng, 3(2): 61–83 (April 1981).

[10] Campbell, F. C.:Chapter1: Inspection methods—Overview and comparison. Inspection of metals: Understanding the basics. ASM International, Pages 1–20 (20) (April 01, 2013). http://www.asminternational.org/documents/10192/1849770/05372_Sample.pdf.

[11] Leach, R.: Chapter6-Surface topography measurement instrumentation. Fundamental principles of engineering nanometrology (second edition), Pages 133-204. http://www.sciencedirect.com/science/article/pii/B9780080964546100065.

[12] Pawlus, R., Śmieszek, M..: The influence of stylus flight on change of surface topography parameters. Precis Eng, 29(3): 272–280 (July 2005).

[13] P. Demircioglu, "Estimation of surface topography for dental implants using advanced metrological technology and digital image processing techniques," Measurement, vol. 48, pp. 43-53, 2014.

[14] T. Jeyapoovan and M. Murugan, "Surface roughness classification using image processing," Measurement, vol. 46, pp. 2065-2072, 2013.

[15] Wang, S.H., Jin, C.J., Tay, C.J., Quan, C., Shang, H.M.: Design of an optical probe for testing surface topography and micro-displacement. Precis Eng, 25(4): 258–265 (October 2001).

[16] Hocken, R.J., Chakraborty, N., Brown, C.: Optical metrology of surfaces. CIRP Ann Manu Technol, 54(2): 169–183 (2005).

[17] Brodmann, R., Gast, Th., Thurn, G., Wirtz, A., Optische Werke G.: Rodenstock. An optical instrument for measuring the surface topography in production control. CIRP Ann Manu Technol, 33(1): 403–406 (1984).

[18] Yim, D.Y., Kim, S.W.: Optical topography measurement of ground surfaces by light scattering. Int J Mach Tools Manu, 30(2): 283–289 (1990).

[19] Sherrington, I., Smith, E.H.: Modern measurement techniques in surface metrology: Part II; optical instruments. Wear, 125(3): 289–308. (1 August 1988).

[20] Whitehouse, D.J.: Surface metrology. Meas Sci Technol, 8(9): 955–972 (1997).

[21] Thomas, T.R.: Rough surfaces. London: Longman (1982).

[22] Ohlidal, M.: Comparison of 2-dimensional Fraunhofer approximation and 2-dimensional Fresnel approximation at analysis of surface-topography by angle speckle correlation. 2. Experimental results. J Mod Opt, 42(10): 2081–2094 (1995).

[23] Nadolny, K., et al.: Laser measurements of surface topography of abrasive tools using measurement system CLI 2000. Przegląd Elektrotechniczny (Elec Rev), 87(9a): 24–27 (2011).

[24] Łukianowicz, C., Karpiński, T.: Optical system for measurement of surface form and topography. Meas Sci Rev, 1(1): 151–154 (2001).

[25] Senchenko, E.S., Chugui, Yu.V.: Shadow inspection of 3D objects in partially coherent light. Meas Sci Rev, 11(4): 104–107 (2011).

[26] Kawate, E., Hain, M.: New scatterometer for spatial distribution measurements of light scattering from materials. Meas Sci Rev, 12(2): 56–61 (2012).

[27] Sherrington, I., Smith, E.H.: Modern measurement techniques in surface metrology: Part I; Stylus instruments, electron microscopy and non-optical comparators. Wear, 125(3): 271–288 (1 August 1988).

[28] K. Tsukada, M. Yoshioka, Y. Kawasaki, and T. Kiwa, "Detection of back-side pit on a ferrous plate by magnetic flux leakage method with analyzing magnetic field vector," NDT & E International, vol. 43, pp. 323-328, 2010.

[29] M. Le, J. Lee, J. Jun, J. Kim, S. Moh, and K. Shin, "Hall sensor array based validation of estimation of crack size in metals using magnetic dipole models," NDT & E International, vol. 53, pp. 18-25, 2013.

[30] S. Mukhopadhyay and G. Srivastava, "Characterisation of metal loss defects from magnetic flux leakage signals with discrete wavelet transform," Ndt & E International, vol. 33, pp. 57-65, 2000.

[31] Dutta, S.M., Ghorbel, F.H., Stanley, R.K.: Simulation and analysis of 3-D magnetic flux leakage. IEEE Trans Magn, 45(4): 1966–1972 (2009).

[32] Krause, T.W., Donaldson, R.M., Barnes, R., Atherton, D.L.: Variation of the stress dependent magnetic flux leakage signal with defect depth and flux density. NDT E Int, 29(2): 79–86 (1996).

[33] G. Kopp and H. Willems, "Sizing limits of metal loss anomalies using tri-axial MFL measurements: A model study," NDT & E International, vol. 55, pp. 75-81, 2013.

[34] Altschuler, E., Pignotti, A.: Nonlinear model of flaw detection in steel pipes by magnetic flux leakage. NDT E Int, 28(1): 35–40 (1995).

[35] Goktepe, M.: Non-destructive crack detection by capturing local flux leakage field. Sens Actuat A, 91(1): 70–72 (2001).

[36] Y. Zhang, Z. Ye, and C. Wang, "A fast method for rectangular crack sizes reconstruction in magnetic flux leakage testing," Ndt & E International, vol. 42, pp. 369-375, 2009.

[37] S. Saha, S. Mukhopadhyay, U. Mahapatra, S. Bhattacharya, and G. Srivastava, "Empirical structure for characterizing metal loss defects from radial magnetic flux leakage signal," Ndt & E International, vol. 43, pp. 507-512, 2010.

[38] M. Le, J. Lee, J. Jun, and J. Kim, "Estimation of sizes of cracks on pipes in nuclear power plants using dipole moment and finite element methods," NDT & E International, vol. 58, pp. 56-63, 2013.

[39] Uetake, I., Saito, T.: Magnetic flux leakage by adjacent parallel surface slots. NDT E Int, 30(6): 371–376 (1997).

[40] C. Coughlin, L. Clapham, and D. Atherton, "Effects of stress on MFL responses from elongated corrosion pits in pipeline steel," NDT & E International, vol. 33, pp. 181-188, 2000.

[41] Amineh, R.K., Koziel, S., Nikolova, N.K., Bandler, J.W., Reilly, J.P.: A space mapping methodology for defect characterization from magnetic flux leakage measurements. IEEE Trans Magn, 44(8): 2058–2065 (2008).

[42] Ravan, M., Amineh, R.K., Koziel, S., etc.: Sizing of 3-D arbitrary defects using magnetic flux leakage measurements. IEEE Trans Magn, 46(4): 1024–1033 (2010).

[43] D. Mukherjee, S. Saha, and S. Mukhopadhyay, "Inverse mapping of magnetic flux leakage signal for defect characterization," NDT & E International, vol. 54, pp. 198-208, 2013.

[44] Chen, Z., Preda, G., Mihalache, O., Miya, K.: Reconstruction of crack shapes from the MFLT signals by using a rapid forward solver and an optimization approach. IEEE Trans Magn, 38(2): 1025–1028 (2002).

[45] N. Gloria, M. Areiza, I. Miranda, and J. Rebello, "Development of a magnetic sensor for detection and sizing of internal pipeline corrosion defects," NDT & E International, vol. 42, pp. 669-677, 2009.